SCIENTIFIC PAPER

PCXMC cone beam computed tomography dosimetry investigations

Aaron Fetin[1,2] · Lucy Cartwright[3] · Jonathan Sykes[4] · Alicja Wach[3]

Abstract

With cone beam computed tomography (CBCT) in image guided radiation therapy being amongst the most widely used imaging modalities, there has been an increasing interest in quantifying the concomitant dose and risk. Whilst there have been several studies on this topic, there remains a lack of standardisation and knowledge on dose variations and the impact of patient size. Recently, PCXMC (a Monte Carlo simulator) has been used to assess both the concomitant dose and dosimetric impact of patient size variations for CBCT. The scopes of these studies, however, have included only a limited range of imaging manufacturers, protocols, and patient sizes. An approach using PCXMC and MATLAB was developed to enable a generalised method for rapidly quantifying and formulating the concomitant dose as a function of patient size across numerous CBCT vendors and protocols. The method was investigated using the Varian on board imaging 1.6 default pelvis and pelvis spotlight protocols, for 94 adult and paediatric phantoms over 6 age groups with extensive height and mass variations. It was found that dose varies significantly with patient size, as much as doubling and halving the average for patients of lower and higher mass, respectively. These variations, however, can be formulated and accounted for using the method developed, across a wide range of patient sizes for all CBCT vendors and protocols. This will enable the development of a comprehensive catalogue to account for concomitant doses in almost any clinically relevant scenario.

Keywords CBCT · PCXMC · Dosimetry · IGRT · OBI · Radiotherapy

Introduction

In image guided radiation therapy (IGRT) the purpose of cone beam computed tomography (CBCT) is to provide an image of the patient's anatomy to be used for correcting their positioning prior to, and/or during, treatment delivery [1]. This technique has become increasingly important as it has enabled safe delivery of highly conformal treatments which require accurate patient positioning. As a result, the technique has seen rapid growth and is now the standard of care, with national surveys in Australia, New Zealand, United Kingdom, United States, and France, all listing kilovoltage (kV) CBCT as the most widely used image guidance

modality [2–5]. As CBCT usage became routine, concern regarding the concomitant dose soon amounted [6]. Numerous studies have since been published examining concomitant dose, in addition to guidelines for the commissioning, management, quality assurance, and safe usage of CBCT [7–14]. Within this body of works, it was shown that the imaging dose is not only significant, but can vary greatly with patient size [9]. The American Association of Physicists in Medicine (AAPM) Task Group (TG) 180 indicated that a single kV CBCT can deliver between 10 and 90 mGy to tissue and 60–290 mGy to bones, depending upon the patient's size [9]. For a treatment containing 35 fractions with daily CBCT, this could result in a significant accumulative dose of up to 3 Gy and 10 Gy delivered to tissue and bone, respectively [9]. The primary concern with concomitant doses of this magnitude is both the increase in cancer effects and the possibility of tissue effects in nearby organs at risk where planned doses may already be approaching their threshold. It should be noted, however, that these figures are representative of an earlier version of the Varian on board imaging (OBI) (v1.3) and have since reduced in newer versions [9].

✉ Aaron Fetin
   aaron.fetin@live.com.au; aaron.fetin@genesiscare.com.au

1   GenesisCare, Lake Macquarie Private Hospital, Gateshead, NSW, Australia

2   The University of Sydney, Camperdown, NSW, Australia

3   Westmead Public Hospital, Westmead, NSW, Australia

4   Blacktown Public Hospital, Blacktown, NSW, Australia

Whilst the dose delivered from image guidance is generally considered justifiable within radiation therapy, there is a clear need for quantification to enable evidence-based decision making. Several methods to estimate the dose have been used including Monte Carlo (MC) techniques (in treatment planning systems or other toolkits e.g. Geant4 or EGSnrc), and measurements with cylindrical phantoms [6]. MC methods can provide individualised patient dose estimates; however, they require significant expertise and time to set-up. They may also require proprietary information regarding the X-ray tube designs from the vendor which may not be available. Additionally, methods using computed tomography dose index (CTDI) phantoms have low collection efficiency and so require 2 or more phantoms to sufficiently capture entire dose profile, which is generally not feasible in most departments [15]. Moreover, methods using CTDI phantoms do not provide individualised patient doses, although size-based corrections could be applied as per AAPM TG 204 [16].

Recently, there have been a few studies that calculate CBCT doses using PCXMC [17–20]. PCXMC is a cost effective and relatively easy to use tool, which allows patient-like doses to be simulated on an intersex anthropomorphic mathematical phantom. The phantom can also be scaled to represent a wide range of patient sizes and ages. As PCXMC is designed for diagnostic X-rays, previous studies utilising it have developed methods that allow it to estimate CBCT doses, however, there are two main limitations with these approaches [17–20]. Firstly, the requirements for an accurate simulation have not been investigated, and secondly, existing approaches either sacrifice accurate representation of the CBCT, or are time consuming and difficult to apply in a wide array of scenarios. The first approach was by Alvarado et al., whereby the CBCT output with a full bowtie filter was approximated by measuring the output at isocentre and taking this value to be constant across the field, neglecting the non-uniformity [17]. A second approach was investigated by Wood et al. whereby the CBCT output with a half bowtie filter was measured in the direction of the gradient and divided into 4 constant fields to represent the non-uniformity [19]. Lastly, the most recent approach was by Rampado et al., whereby the CBCT output with a full bowtie filter was represented as two numerically weighted and superimposed fields; one narrow field to represent the central region, and a wider field to represent the peripheral [20]. In each case, the authors simulated the fields at a discrete set of gantry angles and the results were summed to represent rotation about the patient. Of the three approaches, the method of Alvarado et al. requires the least physical measurements, is easiest to implement in PCXMC, and is the least computationally demanding [17]. It, does, however achieve this at the expense of accurate representation of the CBCT output. In contrast, the method of Wood et al. most accurately represents the CBCT output but requires the

most physical measurements and may require calculations to manipulate the input to suit PCXMC [19]. This renders it cumbersome to use in a wide array of scenarios, whilst also being the most computationally demanding. Lastly, the method of Rampado et al. is a compromise, with accuracy, ease of use, and computational demand somewhere in between the former two methods [20].

Given the limitations in existing approaches using PCXMC, this study develops a method based upon that of Wood et al., by utilising an automated approach in MATLAB and quantifying the requirements for a precise simulation [19]. The automated approach enables PCXMC input data to be generated rapidly to allow various scenarios to be simulated easily without sacrificing accuracy. This method was investigated using the Varian OBI v1.6 default pelvis and pelvis spotlight protocols, for 94 adult and paediatric phantoms over 6 age groups with a range of heights and weights. The aim of this work was to develop the methodology by which a comprehensive set of CBCT doses could be created for any CBCT technique representing a range of patient sizes. This could be used by professionals in radiation therapy to justify concomitant doses, optimise imaging protocols, and for those considering risks associated with the additional imaging dose associated with clinical trials.

Method

Equipment

PCXMC 2.0

PCXMC is a MC program for simulating X-ray examinations that was developed and made available by the radiation and nuclear safety authority of Finland (STUK) [21, 22]. The program uses a mathematical phantom that is adjustable by age, height and mass [21]. The phantom is intersex and representative of both male and female anatomy, providing absorbed dose estimates to 29 organs and tissues, in addition to the effective dose and BEIR VII risk estimates [21].

Within this study the phantom was adjusted to cover a comprehensive range of typical patients across 6 age groups. This included 49 adult and 45 paediatric patients, with size variations including the average, maximum and minimum of population height and mass from national Australian surveys in 1995 and 2007 [23, 24]. Additionally, four extra points were taken for the adult group to include standard deviations of one and two from the mean in both directions. The phantom ages and sizes are summarised in Table 1.

PCXMC requires the user to define the field-size, distance to isocentre (or surface), anode material, anode angle (degrees), total filtration [half value layer in mm of aluminium (HVL mm Al)], a dose quantity, and the number of

Table 1 PCXMC phantom parameters

Age (years)	Total	Height (cm)	Mass (kg)
0	9	46, 50, 54	2.5, 3.5, 4.5
1	9	69, 75, 80	7, 9, 12
5	9	106, 120, 133	18, 24, 32
10	9	135, 150, 165	30, 45, 61
15	9	158, 169, 181	48, 63, 80
18+	45	135, 154, 161, 168, 175, 182, 201	32, 48, 61, 75, 88, 102, 140

Table 2 Varian OBI 1.6 default pelvis and pelvis spotlight protocol parameters [25]

	Pelvis	Pelvis spotlight
Tube voltage (kVp)	125	125
Tube current (mA)	80	80
Pulse width (ms)	13	25
Projections	655	360
mAs per projection	1.04	2
Gantry rotation	360	200
Fan mode	Half	Full
Bowtie filter	Half	Half
$CTDI_w$ (mGy/100mAs)	2.6	3.4

photons to be simulated and their maximum energy (keV). The dose quantity can be specified as air kerma (mGy), dose-area product (mGycm^2), exposure (mR), exposure-area product (Rcm^2), or current–time product (mAs). PCXMC assumes any dose quantity to be constant across the radiation field, hence the need for a work-around to enable it to estimate CBCT doses. In this study, the anode was tungsten with an angle of 14° as per the OBI kV source unit specifications. Additionally, in PCXMC the max photon energy was 150 keV (default) and the number of simulated photons was 20,000 (default) [25]. The remaining parameters were chosen to reflect the CBCT used, as per Table 2.

Varian OBI 1.6

The CBCT used within this study is the Varian OBI 1.6 attached to the Clinac linear accelerator. The protocols used within this study were the default pelvis and pelvis spotlight, the details of which are summarised in Table 2. The pelvis protocol acquires the CBCT over a complete rotation using a half-fan that covers half of the abdomen [25]. In contrast, the pelvis spotlight protocol acquires the CBCT over a partial arc using a full-fan with a reduced field of view (FOV) in order to reduce dose [25]. The pelvis protocol was used to assess the requirements for a precise simulation, whilst the

pelvis spotlight protocol was used for assessing and modelling patient dose as a function of patient size, air kerma and beam quality. In addition, as previously mentioned the anode in the OBI is tungsten, with an angle of 14°.

Unfors raysafe R/F detector

The Unfors 8202031-J R/F detector (Raysafe, Uggledal, Sweden) was used to acquire all physical measurements. This detector was calibrated within the previous year and is traceable to the SP Technical Institute of Sweden. The manufacturer specifications are $\pm 5\%$ for air kerma and $\pm 10\%$ for filtration (mm Al).

CBCT output characterisation

The CBCT was characterised by measuring lateral profiles (in the direction of change with the bowtie filters) of total filtration (mm Al) and air kerma per projection (mGy) using the Unfors R/F detector. Measurements were performed for the pelvis spotlight protocol (full fan, half bow-tie filter) with profile data from Wood et al. being used for the pelvis protocol (half fan, half bow-tie filter) [19]. This data was adopted as the CBCT and imaging protocols used by Wood et al. are the same as in this study, and remeasuring existing data was not necessary for the purposes of developing a proof of concept [19]. Measurements were performed using fluoroscopic mode at a fixed gantry angle with exposure parameters set as described in Table 2. The detector was held by a retort stand placed in the centre of the treatment couch positioned 100 cm from the kV source and orientated such that its length ran perpendicular to anode-heel effect and the bowtie filter direction. The detector was initially placed at isocentre then stepped laterally through the field, with measurements obtained with 200 pulses per position, as to minimise statistical uncertainty. To convert the measured beam quality (HVL mm Al) to total filtration (as required by PCXMC) the online Siemens tool for X-ray spectra simulation available at was used [26]. The tool allowed X-ray spectra to be simulated and the beam quality estimated for a user defined anode, kVp, and total filtration. By running repeated simulations and varying the total filtration, the output beam quality can be plotted as a function of the input total filtration. This allowed equations to be fit that convert beam quality to total filtration for 125kVp with a tungsten anode at an angle of 14°.

PCXMC input with MATLAB

A MATLAB script was used to generate input data to PCXMC for any user defined profiles, projections, rotations, phantom sizes, field sizes, and with isocentre at any point within the phantom. The first step accounts for the
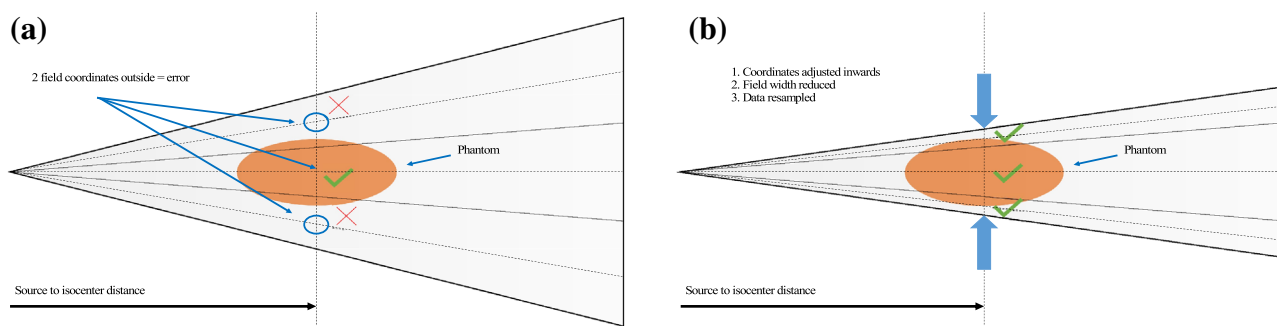
(a)

(b)

Fig. 1 MATLAB script coordinate correction process. **a** Coordinates prior to correction. **b** Coordinates following correction

non-uniformity of the CBCT field, which PCXMC does not simulate by default. The method utilises a discrete integration, whereby the script divides the field into a series of equally sized narrow sub-fields as depicted in Fig. 1. Each sub-field is then independently simulated in PCXMC, and the sum of results yields a total dose estimate. Each of these sub-fields are represented by a 3D coordinate and five scalars. The 3D coordinate represents the position of the field on the phantom, where the coordinate is at the geometric centre the field. The 5 scalars include the distance to the coordinate from the source of radiation, the field size (ΔX and ΔY), the total filtration, and the air kerma. In effect, the way PCXMC is simulating the off-axis fields is by moving the position of the source such that the centre of the defined field is aligned with the central axis of the source at the defined distance. The values for total filtration and air kerma are then derived from the measured profiles based on the sub-fields position. Additionally, each coordinate was taken to have the same distance of 100 cm from the source. This approach yields source offsets which are always in the same plane, normal to the central axis and parallel to the defined field size. Whilst simple, this does result in an error due to the inverse square law (ISL), which is discussed further in the uncertainty section below. To allow for gantry rotation, the coordinates are rotated in the transverse plane by a 2D rotational matrix, as to obtain coordinates for all user defined projection angles. To reduce simulation run-time the PCXMC calculations were approximated by reducing the number of projections and scaling the air kerma per projection as to maintain a constant total air-kerma for the scan.

Additionally, PCXMC does not allow the central coordinate of a sub-field to be defined outside of the phantom surface. This is primarily a problem for the lateral coordinates that tend to fall outside the phantom surface as the field is rotated about the patient. In a study by Wood et al., it appears the authors had chosen to manually remove the coordinates where this was a problem [19]. However, a method to allow for automated simulation of a wide array of scenarios required a different approach. As such, an algorithm was
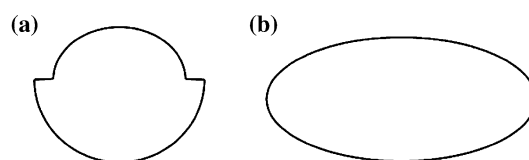

Fig. 2 PCXMC phantom cross sections. **a** Transverse head slice. **b** Transverse torso slice

developed within MATLAB that checks if a coordinate and the entirety of its field are outside of the phantom, removing them if so. However, if a coordinate has fallen outside of the phantom but some of the field remains within, that coordinate is moved to the surface, with field width reduced and the field data resampled. This process is depicted in Fig. 1.

This process was developed to work for the head and torso cross sections of any phantom in PCXMC, as depicted in Fig. 2. The torso cross section was modelled as an ellipse, whilst the head was modelled as two ellipses with distinct radii, one above the y-axis and one below. The dimensions of these were manually recorded from PCXMC and are used by the script to adjust the sub-fields for each phantom uniquely. Moreover, as the PCXMC coordinates of a given organ change with patient size, the geometric centre for each organ of interest was uniquely recorded for each phantom size considered, as to ensure accurate field positioning.

As an example, Fig. 3 illustrates the capacity of the script to handle various user defined scenarios. In Fig. 3, the thick incomplete concentric circles (red) are the traced position of each sub-fields coordinate as it is rotated about the phantom, the thin incomplete concentric circles (blue) are the traced position of the boundary between adjacent sub-fields, and the complete elliptical outline (black) represents the surface of the phantom cross section as in Fig. 2. The example depicts the coordinates for a half-fan CBCT scan that is off-centre on an adult's torso. The field is divided into 4 unevenly sized sub-fields for 250 projections over a 250° rotation. The left image shows the coordinates before correction, whilst the right image shows the coordinates after correction.
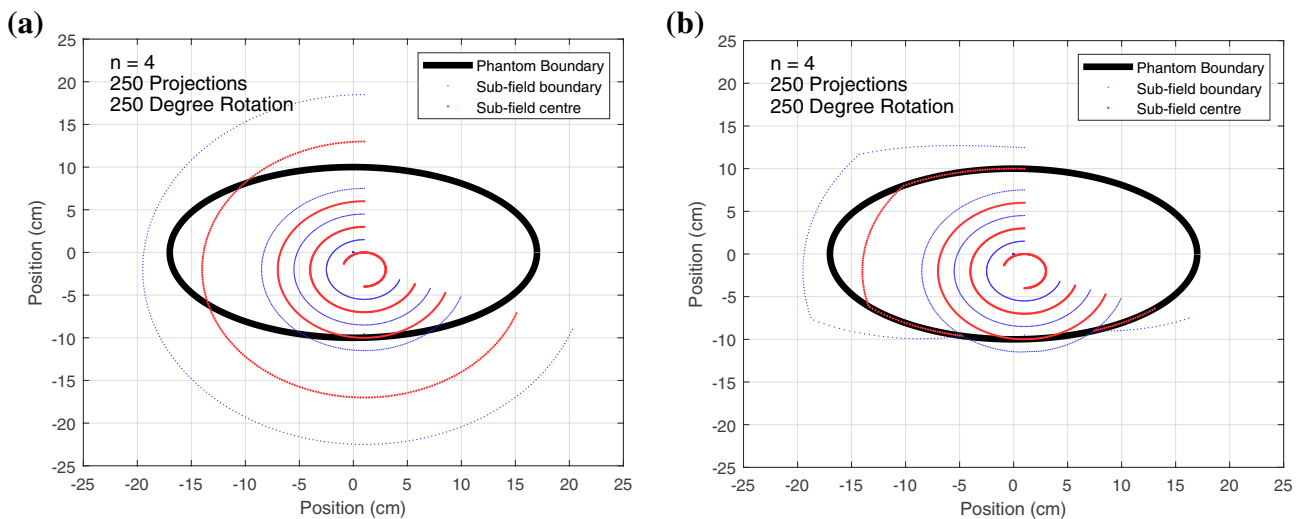
(a)

(b)

Fig. 3 Example of the MATLAB coordinate correction for an off-centre half-fan CBCT of a torso cross-section. The field is divided into 4 uneven sub-fields, with 250 projections taken over a 250° rotation. **a** Original fields prior to correction. **b** Amended fields following correction

Table 3 Field size specifications by age

Age group	ΔX	ΔY
18+	26.4	19.98
15	23	17
10	19	14.5
5	15.5	11.5
1	12	9
0	9	6

Dose as a function of patient size, beam quality and air kerma

The effective dose and absorbed doses to each of the 29 organs from the pelvis spotlight protocol were obtained in PCXMC for all phantoms outlined in Table 1. The scan acquisition parameters as provided by Varian were used in each case, except for field size, which was adjusted to provide the same internal view for each age group, as it does for adults. The adjusted field sizes for each age group are given in Table 3. In all cases the phantom was positioned with the isocentre geometrically centred within the prostate as per a standard prostate examination. The number of sub-fields and projections used were 15 and 8, respectively. These parameters were chosen as they yielded a convergence within 1.5% of the baseline and a moving standard deviation within 1%, as discussed in the Simulation Uncertainty section of the Results.

To explore modelling the resulting doses, two models were used. The first models doses as a function of equivalent diameter, where equivalent diameter is given by Eq. 1 as per AAPM TG 204 [16].

$$d_{eq} = \sqrt{\text{Width} \times \text{Depth}} \tag{1}$$

However, while this model accounts for patient size and yields simulated doses that are likely a reasonable estimate for most similarly performing CBCTs, significant differences could arise for CBCTs that have notable variations in beam quality, air kerma, or scan acquisition parameters.

To develop a model that accounts for air kerma, beam quality, patient height and patient mass, all simulations were repeated with beam quality varying from 3.5 mm Al to 9 mm Al in steps of 0.5 mm Al. Firstly, given that dose is proportional to air-kerma, variations can be accounted for as per Eq. 2, where K_0 and K are the reference and field air kerma (defined at isocentre), Q_0 and Q are the reference and field beam quality (defined at isocentre), h is the patient's height, and m is the patient's mass. Additionally, $E(K_0, Q_0, h, m)$ is the average absorbed or effective dose for the reference air kerma, while $E(K, Q, h, m)$ is the adjusted average absorbed or effective dose for the field air kerma.

$$\frac{E(K, Q_0, h, m)}{E(K_0, Q_0, h, m)} = \frac{K}{K_0} \tag{2}$$

Secondly, the relationship between average dose and beam quality can be modelled as logarithmic as per Fig. 4. However, the constants depend on the patient's size, as also seen in Fig. 4. To account for patient size dependence, the curve fit for each patient size can be normalised by the dose at the reference beam quality. This produces an almost equal result for phantoms of all sizes within a given age group, as per Fig. 5. The overall relationship between average dose, beam quality and air kerma is therefore defined by Eq. 3,

Fig. 4 Effective dose from the pelvis protocol as a function of beam quality for several adult phantoms depicting the height/mass dependence
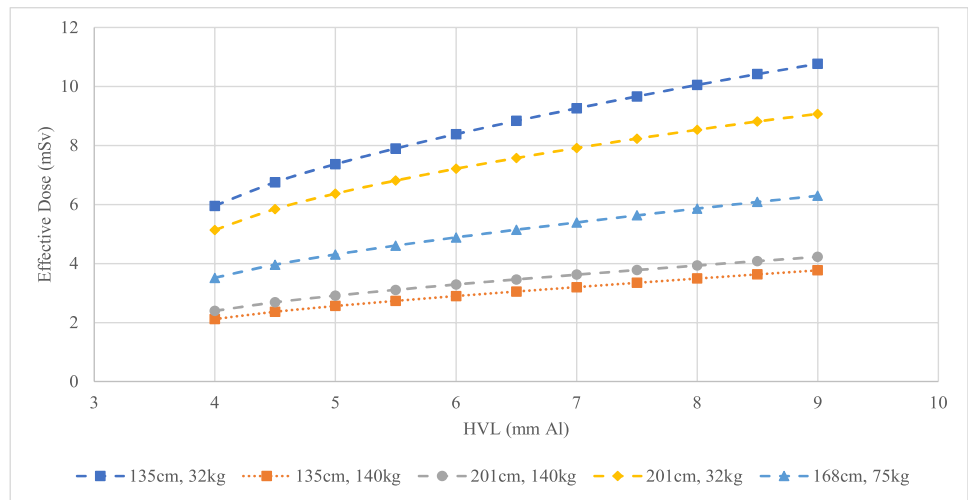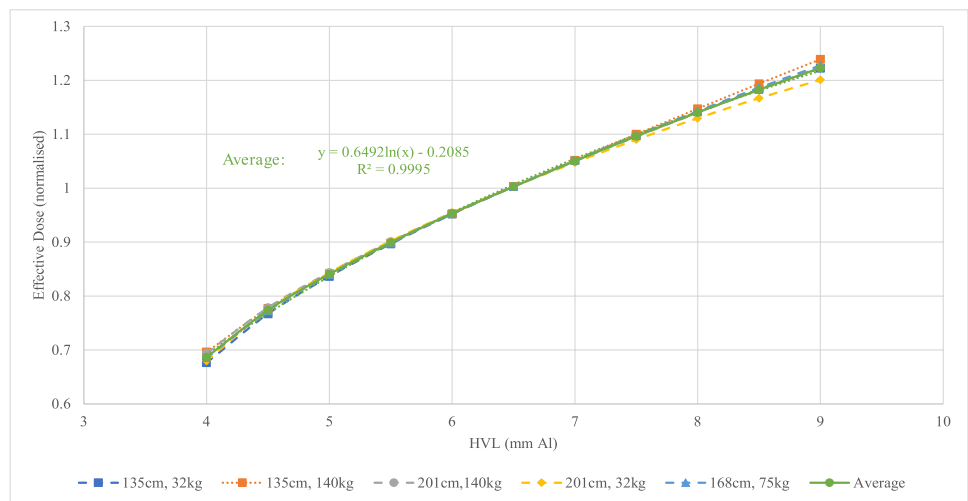

Fig. 5 Normalised effective dose from the pelvis protocol as a function of beam quality for several adult phantoms

where a and b are constants found by fitting the logarithmic function to the normalised dose curves.

$$\frac{E(K, Q, h, m)}{E(K_0, Q_0, h, m)} = \frac{K}{K_0}[a \cdot \ln(Q) + b] \tag{3}$$

The dependency on constants in Eq. 3 can partially be reduced by noting that as per normalisation conditions:

$$a \cdot \ln(Q_0) + b = 1 \tag{4}$$

Therefore, substituting b from Eq. 4 into Eq. 3, yields the simplified result in Eq. 5:

$$\frac{E(K, Q, h, m)}{E(K_0, Q_0, h, m)} = \frac{K}{K_0}\left[a \cdot \ln\left(\frac{Q}{Q_0}\right) + 1\right] \tag{5}$$

Simulation uncertainty

To quantify the requirements for a precise simulation, a baseline was first established using the pelvis protocol, with data utilised from Wood et al. [19]. A simulation was run with the field divided into 112 sub-fields, each simulated in 3° intervals over 360° (120 projections each). This resulted in over 13,000 narrow beams to be simulated with a run-time of over 24 h. The phantom size was chosen to represent an average adult male with a height and mass of 175 cm and 75 kg, respectively.

To assess the precision as a function of the number of sub-fields and projections used, 120 more simulations were run whilst varying simulation parameters. First, simulations were repeated with a fixed number of sub-fields (3, 6, and 30) whilst increasing the number of projections in steps of 1, from 1 to 20. The same process was then repeated, this time with a fixed number of projections (8, 16, and 32) whilst increasing the number of sub-fields in steps of 1, from 1 to

20. The results were then normalised to the baseline and a moving standard deviation computed (window size of 5). As the neighbours of a given point exhibit fluctuations relative to the central point, a moving standard deviation was used to allow the level of convergence to be quantitatively assessed. This ensured that not only is the chosen point sufficiently close to the baseline but was also selected in a region that had consistently converged to that baseline.

To then estimate the combined uncertainty in dose, Eq. 5 is first rearranged to give an adjusted dose estimate as:

$$E(K, Q, h, m) = E(K_0, Q_0, h, m) \frac{K}{K_0} \left[a \cdot \ln\left(\frac{Q}{Q_0}\right) + 1 \right] = E(K_0, Q_0, h, m) K'(K) Q'(Q), \qquad (6)$$

where

$$K'(K) = \frac{K}{K_0} \qquad (7)$$

$$Q'(Q) = a \cdot \ln\left(\frac{Q}{Q_0}\right) + 1 \qquad (8)$$

The fractional uncertainties in the simulated dose, air kerma measurement and filtration measurement can then be added in quadrature:

$$\frac{\Delta E(K, Q, h, m)}{E(K, Q, h, m)} = \sqrt{\frac{\Delta E(K_0, Q_0, h, m)^2}{E(K_0, Q_0, h, m)} + \frac{\Delta K'^2}{|K'|} + \frac{\Delta Q'^2}{|Q'|}} \qquad (9)$$

The first term of Eq. 9 accounts for the uncertainty in MC as quoted by PCXMC (e_{PCXMC}), the uncertainty introduced by simplifying the field into a discrete number of projections (e_{proj}), and the uncertainty due to a lack of off-axis distance corrections (e_{dist}). The first term of Eq. 9 can be written as:

$$\frac{\Delta E(K_0, Q_0, h, m)^2}{E(K_0, Q_0, h, m)} = e_{PCXMC}^2 + e_{simplification}^2 + e_{dist}^2 \qquad (10)$$

e_{PCXMC}^2 is quoted by PCXMC post-simulation, and $e_{simplification}^2$ is to be determined following assessment of the requirements for simulation precision as described above. e_{dist} was estimated as the maximum absolute percentage difference between ISL corrections for the patient with the largest equivalent diameter when using source to coordinate distances of 100 cm and a corrected value. The estimates are conservative as the patient with the largest equivalent diameter is used with values calculated at the most distal points of the most off axis field possible. The patient with the largest effective diameter has a width of 54.68 cm and a depth of 31.30 cm. For a gantry angle of 0°, the most off axis field possible is displaced laterally from the patient's centre by half the patient's width (27.34 cm), which has a source to coordinate distance of 103.67 cm. The most distal points relative to this field lie anteriorly or posteriorly at half the patient's depth (15.65 cm). Whilst these points do lie outside of the patient, they provide a conservative estimate of the worst-case-scenario. In this scenario, the maximum absolute percentage difference between ISL corrections for source to coordinate distances of 100 cm and 103.67 cm was 1.3%. Additionally, this calculation was repeated for a gantry angle of 90°, yielding a maximum absolute percentage difference of 0.9%. As such, e_{dist} was taken to be 1.3%.

The second and third terms of Eq. 9 account for uncertainty in the measured air kerma and filtration, respectively. The Unfors has a quoted uncertainty of 5% and 10% when measuring air kerma and filtration, respectively. In addition, positional uncertainty during measurement will also contribute to uncertainty in air kerma due to the ISL. Taking a conservative assumption that the error in vertical position and off-axis position are both ± 0.5 cm, the maximum ISL correction for the most off-axis point measured (14 cm) is 1.1%. Adding the uncertainties for air kerma in quadrature, the fractional uncertainties for air kerma and filtration are given by:

$\frac{\Delta K'}{|K'|} = 0.051$, $\frac{\Delta Q'}{|Q'|} = a \, 0.1$, where the value of a is taken as the value determined when fitting the logarithmic equation, where available. To estimate uncertainty in cases where a was not determined, a conservative estimate of $a = 1$ was used. This value was considered conservative as it is considerably larger than the value determined in other cases.

Results

CBCT output characterisation

The HVL and air kerma for the pelvis spotlight protocol at isocentre for a single projection were measured to be $5.99 \pm 10\%$ mm Al and $0.113 \pm 5.1\%$ mGy/mAs, respectively. The measured HVL at isocentre was consistent with the average of previously published values for a pelvis spotlight [27–32]. The measured profiles of total filtration and air kerma are depicted in Fig. 6a, whilst Fig. 6b depicts the equations used to convert HVL (mm Al) to total filtration (mm Al). The profiles for the pelvis protocol are not shown as they were adopted from a paper by Wood et al. [19].
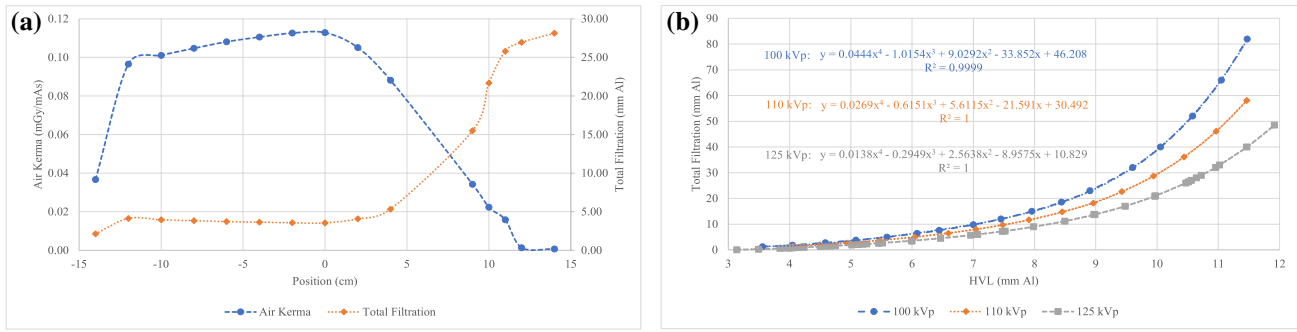
Fig. 6 **a** Pelvis spotlight total filtration (mm Al) and air kerma (mGy/mAs) profiles. **b** Plot of the equations to convert HVL to total filtration for 100 kVp, 110 kVp and 125 kVp
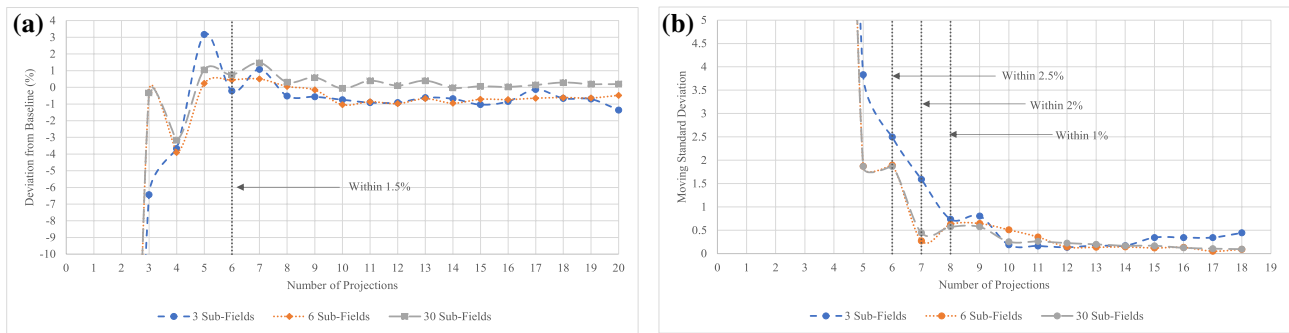

Fig. 7 **a** Deviation from baseline of effective dose as a function of the number of projections for a default prostate protocol. **b** The moving standard deviation using a window size of 5 in the normalised effective dose as a function of the number of projections for a default pelvis protocol
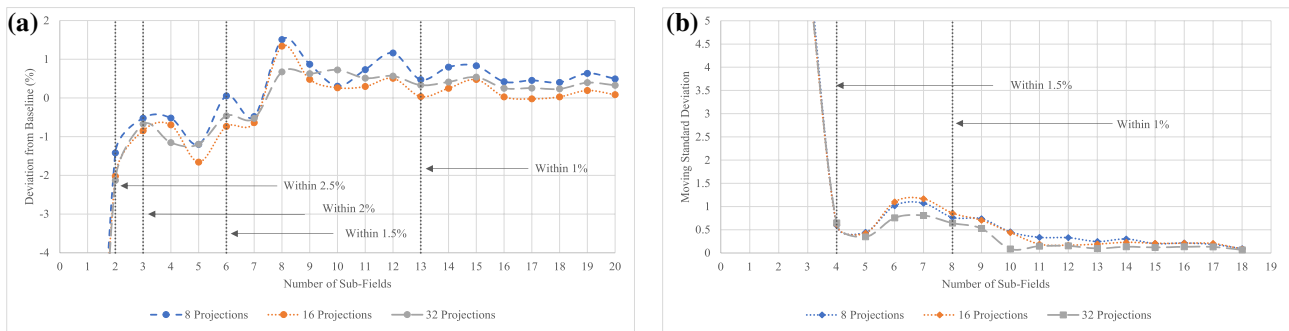

Fig. 8 **a** Deviation from baseline of effective dose as a function of the number of sub-fields for a default prostate protocol. **b** The moving standard deviation using a window size of 5 in the normalised effective dose as a function of the number of sub-fields for a default pelvis protocol

Simulation uncertainty

The effective dose (normalised to the baseline) as a function of the number of projections and sub-fields for the pelvis protocol are given in Figs. 7a and 8a, respectively. Additionally, the moving standard deviation with a window size of 5 for the effective dose as a function of the number of projections and sub-fields for the pelvis protocol are given

in Figs. 7b and 8b, respectively. Within these figures the number of sub-fields or projections required to achieve a given percentage of precision is indicated by a vertical line.

In this study, 15 sub-fields and 8 projections were used for a full-fan CBCT, while 8 sub-fields and 8 projections were used for a half-fan CBCT. These parameters were chosen were the minimum for which the average effective dose converged within 1.5% of baseline with a moving

Table 4 Effective dose (mSv) from pelvis spotlight protocol for adults aged 18+ years

		Height (cm)						
		135	154	161	168	175	182	201
Mass (kg)	32	6.4±0.6	5.8±0.6	5.7±0.6	5.6±0.6	5.4±0.5	5.3±0.5	5.2±0.5
	48	4.9±0.5	4.6±0.5	4.5±0.5	4.5±0.4	4.4±0.4	4.4±0.4	4.3±0.4
	61	4.0±0.4	3.8±0.4	3.8±0.4	3.8±0.4	3.7±0.4	3.7±0.4	3.7±0.4
	75	3.3±0.3	3.2±0.3	3.2±0.3	3.2±0.3	3.2±0.3	3.2±0.3	3.2±0.3
	88	2.8±0.3	2.8±0.3	2.8±0.3	2.8±0.3	2.8±0.3	2.8±0.3	2.8±0.3
	102	2.4±0.2	2.4±0.2	2.4±0.2	2.4±0.2	2.4±0.2	2.4±0.2	2.4±0.2
	140	1.6±0.2	1.6±0.2	1.7±0.2	1.7±0.2	1.7±0.2	1.7±0.2	1.8±0.2

Table 5 Absorbed prostate dose (mGy) from pelvis spotlight protocol for adults aged 18+ years

		Height (cm)						
		135	154	161	168	175	182	201
Mass (kg)	32	29.0±3.2	32.2±3.5	32.5±3.5	33.9±3.7	34.3±3.7	34.5±3.7	36.8±3.9
	48	21.4±2.4	23.8±2.6	24.8±2.7	25.7±2.8	26.7±2.9	27.3±2.9	29.4±3.1
	61	16.7±1.9	19.1±2.1	20.1±2.2	21.0±2.3	21.7±2.4	22.4±2.4	24.4±2.6
	75	13.5±1.5	15.6±1.7	16.4±1.8	17.2±1.9	17.9±2.0	18.6±2.0	20.6±2.2
	88	11.2±1.3	13.1±1.5	13.7±1.5	14.3±1.6	15.1±1.7	15.8±1.7	17.5±1.9
	102	9.3±1.1	10.9±1.2	11.5±1.3	12.1±1.3	12.9±1.4	13.4±1.5	14.9±1.6
	140	5.9±0.7	7.1±0.8	7.6±0.9	8.0±0.9	8.5±0.9	9.0±1.0	10.2±1.1

Table 6 Effective (mSv) and absorbed organ (mGy) doses from pelvis spotlight across various age groups

Age group		Effective dose (mSv)	Absorbed dose (mGy)					
		ICRP103	Prostate	Bladder	Testes	Uterus	Ovaries	Colon
18+	Min	1.6±0.2	5.9±0.7	5.2±0.5	4.3±0.4	4.1±0.4	3.4±0.5	3.8±0.4
	Av	3.4±0.3	18.8±2.1	16.4±1.7	12.8±1.3	10.3±1.1	8.4±1.1	7.9±0.8
	Max	6.4±0.6	36.8±3.9	31.8±3.2	25.0±2.6	25.6±2.6	23.8±3.0	14.0±1.4
15	Min	2.8±0.3	13.2±1.9	11.9±1.4	10.9±1.3	6.6±0.8	5.6±0.9	6.3±0.7
	Av	3.5±0.4	18.8±2.6	16.7±2.0	14.6±1.8	8.9±1.0	7.3±1.1	7.8±0.9
	Max	4.2±0.5	25.1±3.4	21.8±2.6	18.2±2.2	12.3±1.4	9.6±1.5	9.5±1.1
10	Min	2.9±0.3	13.4±2.0	12.7±1.5	12.0±1.7	6.7±1.0	5.7±0.9	6.7±0.8
	Av	3.9±0.4	21.9±3.2	19.7±2.3	17.9±2.5	9.7±1.4	8.2±1.3	8.8±1.0
	Max	5.0±0.6	31.8±4.6	27.7±3.2	24.1±3.4	15.2±2.1	12.0±1.8	11.3±1.3
5	Min	3.8±0.4	19.8±2.8	17.6±2.0	17.3±2.3	8.2±1.2	6.9±1.1	8.6±1.0
	Av	4.6±0.5	28.0±3.9	24.5±2.8	23.4±3.1	10.8±1.6	9.2±1.5	10.4±1.2
	Max	5.5±0.6	37.3±5.1	31.2±3.6	29.5±3.9	15.3±2.1	12.7±2.0	12.6±1.4
1	Min	5.3±0.6	28.6±3.8	26.3±3.1	27.4±3.5	11.3±1.6	9.7±1.7	11.7±1.3
	Av	6.1±0.7	35.5±4.7	32.6±3.8	33.5±4.3	14.8±2.1	11.9±2.1	13.6±1.6
	Max	7.0±0.8	42.6±5.6	38.8±4.5	38.9±5.0	21.6±3.0	14.9±2.7	15.7±1.8
0	Min	6.2±0.7	34.7±4.3	33.2±3.9	36.0±4.4	11.2±1.4	9.6±1.8	13.8±1.6
	Av	7.1±0.8	42.9±5.3	39.9±4.7	42.7±5.2	13.9±1.7	11.2±2.1	15.6±1.8
	Max	8.1±0.9	51.1±6.3	46.9±5.5	49.7±6.1	19.1±2.3	13.9±2.7	17.8±2.1

Fig. 9 Absorbed prostate dose (mGy) from the default pelvis spotlight protocol as a function of equivalent diameter for 49 adult and 45 paediatric phantoms
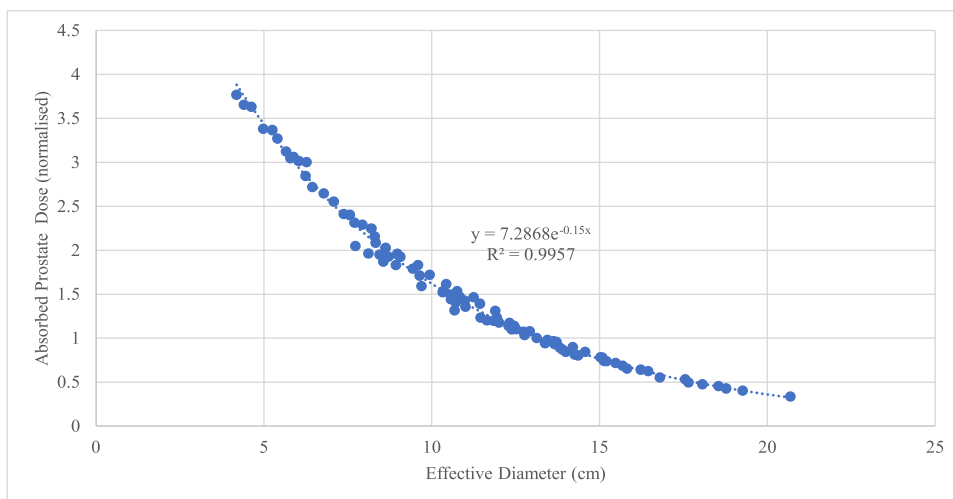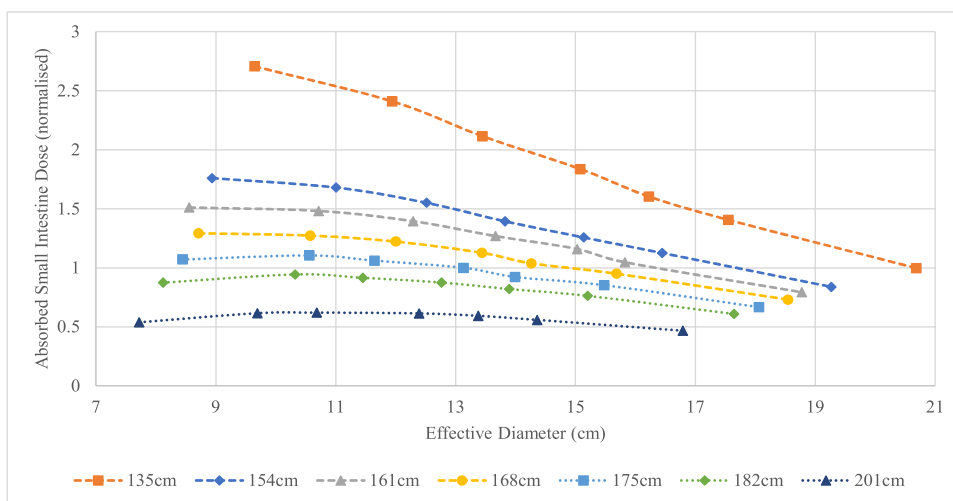

Fig. 10 Absorbed small intestine dose (mGy) from the pelvis spotlight protocol as a function of equivalent diameter for 49 adult phantoms with height/mass dependency illustrated

standard deviation less than 1%. For the full fan the number of sub-fields was increased to 15 to account for the increased width of the field whilst maintaining the same sub-field spacing. The larger of these two values (1.5%) is taken as $e^2_{\text{simplification}}$ for the purposes of calculating combined uncertainty in dose.

Dose as a function of patient size, beam quality and air kerma

The effective dose and absorbed prostate dose from the pelvis spotlight protocol for the 49 adult phantoms is summarised in Tables 4 and 5, respectively. Table 6 also lists the minimum, average and maximum doses recorded across age groups for the pelvis spotlight. Additionally, the absorbed dose to the prostate and small intestine as a function of equivalent diameter are given in Figs. 9 and 10, respectively.

Based on the simulated data, the constants required by Eq. 5 for the pelvic spotlight were found to be:

$$a = 0.820, \; K_0 = 0.113 \, \frac{\text{mGy}}{\text{mAs}} \pm 5.1\%, \; Q_0 = 5.99 \, \text{mm Al} \pm 10\%$$

It should be noted that these values are only appropriate for the adult age group (18 + years). This is as variations in beam quality following normalisation are too significant across age groups, and unique factors are required for each. It is, however, still possible to apply the simplified relationship in Eq. 2, provided beam quality does not vary significantly from the reference conditions.

Table 7 Recommended PCXMC parameters for a half-fan scan over 360°

Level of precision	Number of sub-fields	Number of projections	Deviation from base-line (%)	Moving standard deviation (%)
Minimum	4	6	2	2.5
Recom-mended	8	8	1.5	1
Maximum	13	11	1	0.5

Discussion

Simulation uncertainty

When assessing simulation precision as a function of the number of projections and sub-fields for the pelvis protocol, Figs. 7 and 8 indicate that the minimum number of projections and sub-fields that could reasonably be used for a 360° half fan scan is 4 and 6, respectively. These parameters result in convergence to baseline within 2%, with a moving standard deviation within 2.5%. It could be argued that Figs. 7 and 8 indicate 2 sub-fields and 6 projections to be acceptable, as they yield convergence to baseline within 3%. However, the moving standard deviation at this point is still quite high, and so the minimum recommendation is 4 sub-fields and 6 projections. This results in 24 narrow beams to be simulated, which with the system utilised; a Microsoft Windows 10 Home edition (64-bit), with an Intel Core i9-6700 T CPU @ 2.80 GHz and 8 GB RAM; has an average run-time of 2.7 min. To obtain a result of higher precision requires the number of sub-fields and projections for a half fan scan both to be 8. This is consistent with a convergence to baseline within 1.5% and a moving standard deviation within 1%, with an approximate run-time of 7.2 min. If further precision was desired, the sub-fields and projections can be increased to 13 and 11, respectively. This yields convergence to baseline within 1% and a moving standard deviation within 0.5%. However, over the range considered (1 to 20) further increases offer no significant gains in precision, whilst significantly increasing run time. The recommendations resulting from this study are summarised in Table 7. As per Table 7, the minimum number of sub-fields and projections recommended for a half fan would be 4 and 6, respectively. This validates the original method used by Wood et al. where the authors used 4 sub-fields and 8 projections. In the case of a full fan acquisition mode, it was assumed that to maintain the same degree of precision would require $2n - 1$ sub-fields, where n is the number of sub-fields used for the half fan mode. The reasoning here is that if n sub-fields are required for a given precision over the gradient induced by a half-bowtie filter, $2n - 1$ are required over the full bowtie gradient. This maintains the same resolution of sampling, assuming the central point is shared.

Generally, the largest source of uncertainty is associated with the use of the Unfors detector for measuring filtration and beam quality, contributing 10% and 5.1% respectively. When all known uncertainties are substituted into Eq. 9, the minimum, average and maximum uncertainties for dose estimates for adults were approximately 9.9%, 10.8% and 14.3%, respectively. Additionally, the minimum, average and maximum values of uncertainty from the MC (e_{PCXMC}) were approximately 2.0%, 4.6% and 10.5%, respectively. Across all the remaining age groups, the minimum, average and maximum uncertainties in doses were approximately 11.4%, 12.4% and 19.3%, respectively. Additionally, across all the remaining age groups, the minimum, average and maximum values of uncertainty from the MC (e_{PCXMC}) were approximately 2.0%, 5.1% and 15.6%, respectively. It is worth noting that in most cases, the higher uncertainties in the MC (e_{PCXMC}) are associated with ovarian dose estimates, and that in general, uncertainty increases as both patient age and equivalent diameter decrease.

There are potential refinements in the method described here that are worthy of further investigation. Firstly, only evenly spaced sub-fields were considered, rather than using sparsely spaced sub-fields to increase resolution where there is highest gradient in the fluence profile, as was done by Wood et al. [19]. A possible solution would be to computationally allocate sub-fields based on the 1st and 2nd derivatives, such that divisions are allocated with emphasis on the high gradient and non-linear regions. This could have the possibility of offering a further reduction in run-time, or more accurate representation of the CBCT field. Secondly, precision was only assessed directly with the half fan mode, whilst values for full fan mode were assumed to be $2n - 1$. Thirdly, the uncertainty arising from a lack of ISL corrections could easily be resolved via simple application of Pythagoras. This however will not account for the fact that it is not possible for PCXMC to truly simulate the divergency of the CBCT. Additionally, these values were only assessed for a single imaging mode (default pelvis). As such, further study would be warranted to validate the assumptions, using both fan modes and across various imaging protocols. Additionally, future works would be warranted to validate the calculations by measurement in an anthropomorphic phantom. However, as this method is an adaptation of that of Wood et al., who had performed such a validation, the method used herein can be assumed to be valid, whilst still warranting further investigation [19].

Dose as a function of patient size, beam quality and air kerma

The assessment of effective and absorbed doses as a function of patient size for the pelvis spotlight protocol, as can be seen in Tables 4, 5, and 6, show significant variations with patient size. Doses can double or halve with patient size when compared to the average within a given age group for a given imaging protocol. Across the range of typical adult phantoms considered the effective dose from the pelvis spotlight varied from 1.62 to 6.39 mSv, with an average of 3.44 mSv. Whilst within the paediatric groups, the range was from 4.21 to 8.07 mSv. In all age groups the highest dose was recorded in the prostate with a range of 5.85–51.13 mGy. However, the pelvis spotlight protocol would never be applied to a paediatric case without first adjusting the acquisition settings appropriately. The large range in doses recorded indicate the clear need to optimise image acquisition settings to account for patient size variations. Without optimisation, the absorbed dose to the prostate for an adult receiving 35 fractions daily CBCT could be between 0.2 and 1.3 Gy. Such numbers indicate that the cumulative dose could be a significant fraction of the prescribed dose and a significant addition to the dose to organs at risk which may have a planned dose already near its threshold. Additionally, using the risk coefficient for adult populations ($0.041Sv^{-1}$) from the International Commission on Radiological Protection (ICRP) Publication 103, the risk of secondary induced cancers in adults undergoing 35 fractions could be as high as 0.9% [33]. Whilst such risk may be justifiable for patients undergoing necessary radiation therapy, it is worth considering the lowest estimate of risk could be 0.2%, further illustrating the potential benefit of optimising image quality and dose [33]. Additionally, it is worth noting that this does not consider the potential tissue effects of CBCT [34].

There are several ways this method can be used within the clinic. Firstly, it can be used to make estimations of the imaging doses associated with a given treatment regime or clinical trial. This will allow clinics to assess the risk and make necessary adjustments, whilst aiding in evidence-based decision making. Another possibility is to apply the results in the development of size-based imaging protocols. For example, Wood et al. studied imaging noise as a function of patient size and used this to develop sized-based categories [18]. This provides information as to when imaging parameters could be safely increased to improve image quality, or reduced when imaging quality was more than sufficient [18]. Lastly, with the high resolution of the data obtained, it is possible to fit multivariable functions, tabulate doses, and/or develop equations for estimating patient doses, as was the primary focus of this study.

The resulting doses were first modelled as an exponential function of equivalent diameter, as was reported by Rampado et al. and AAPM TG 204 [16, 20]. As per Fig. 9, this approach works well for organs near the isocentre, such as the prostate, testes, and bladder. However, as per Fig. 10, this approach does not work for organs at the periphery of the field, rendering the method unsuitable for estimating effective doses. A second option is to fit multivariable functions to the results and model dose as a polynomial function of height and weight, however, in practice as many as 8 terms need to be included yielding cumbersome and unpractical formulae. A more practical implementation is to tabulate the results, as seen in Tables 4 and 5. The data can then be interpolated for a specific estimate, with a corrective formula applied for variations in tube output and/or beam quality, if necessary, as per Eqs. 2 and 5. This would result in a set of lookup tables for each imaging protocol, including one for the effective dose and one for the average absorbed dose to *each* organ of interest. The primary purpose would be to allow fast and accurate estimates of patient-like doses across vendors and imaging protocols, without the need for further simulations. Another clinic need only measure the air kerma and beam quality at isocentre, then use those as input to Eqs. 2 and 5 to account for variations if necessary.

For example, to estimate the absorbed dose to the prostate for a 172 cm, 95 kg adult patient undergoing a pelvic spotlight examination, assume we had measured our tube output and beam quality to be 50% and 10% higher at isocentre than the references, respectively. We could first interpolate to find the approximate absorbed dose from Table 5, yielding an absorbed dose (D_0) of 13.7 mGy. We could then substitute all known values into Eq. 5 as such:

$$D = \frac{K}{K_0} D_0 \left[a \cdot \ln\left(\frac{Q}{Q_0}\right) + 1 \right]$$

$$= 1.5 \cdot 13.7 \, \text{mGy} \cdot [0.819 \cdot \ln(1.1) + 1]$$

$$\sim 22.16 \text{mGy}$$

This result is in a good agreement with the result obtained through direct simulation of this scenario, which is 21.98 mGy (within 1%).

While the results showcase the usefulness of the method and what can be achieved, there are several limitations. Firstly, Varian OBI 1.6 has become obsolete in most clinics within Australia. As a result, the data derived may not be directly useful for most clinics, but rather serves as a proof of concept for what can be achieved for a more modern machine. Particularly the ability for one clinic to undertake such measurements and develop generalised formulae for inter-clinical use. It also serves as an indication

of the kind of doses one may expect and provides evidence that variation of dose with patient size is significant. Secondly, the simulations for paediatric and patients of higher mass utilised the default parameters, except for field size which was adjusted across age groups. However, realistically the field size is rarely adjusted, the kV would be lower for paediatrics, and inversely the kV would be higher for patients of higher mass. Lastly, whilst PCXMC provides doses to a wide array of organs, it has no capacity to provide doses in any other format than an average to the volume, such as a point dose. While this can provide an indication of the average dose, it does not yield information such as the peak dose to an organ.

As a result, the intent for future work is threefold: (1) Assess simulation precision for both fan modes at different sections of the body. (2) Validate the results with an anthropomorphic phantom. (3) Comprehensively catalogue a wide range of patient like doses across all current generation vendors and protocols. The end goal of which is to enable dose estimates to be readily obtained for all patients in almost any clinically relevant scenario.

Conclusion

In conclusion, an approach using MATLAB was developed to allow for typical patient doses for CBCT to be simulated with PCXMC. The approach is an adaptation of the method of Wood et al. and allows for patient doses to be tabulated as a function of patient size, with correction factors that can account for variations in tube output and beam quality [19]. The approach was investigated using 2 Varian OBI pelvis protocols, showing significant variations in patient doses with size and the need for imaging doses to be optimised. The method provides clinics with a means of assessing patient doses and aiding in the development of protocols that are optimised to reduce the burden of image guidance.

Declarations

Conflict of interest All authors certify that they have no affiliations with or involvement in any organization or entity with any financial or non-financial interest in subject matter or materials discussed in this study.

Ethical approval All authors certify that this study does not contain any research with animal or human participants conducted by any of the authors.

Consent to participate All authors certify that this study does not contain any research with human participants conducted by any of the authors.

Consent for publication All authors certify that this study does not contain any private or sensitive materials pertaining to any individual or entity.

References

1. Sterzing F, Engenhart-Cabillic R, Flentje M, Debus J (2011) Image-guided radiotherapy: a new dimension in radiation oncology. Dtsch Arztebl Int 108(16):274–280. https://doi.org/10.3238/arztebl.2011.0274

2. Ariyarante H, Chesham H, Roberto A (2016) Image-guided radiotherapy for prostate cancer in the United Kingdom: a national survey. Br J Radiol. https://doi.org/10.1259/bjr.20160059

3. Batumalai V et al (2016) Survey of image-guided radiotherapy use in Australia. J Med Imaging Radiat Oncol 61(3):394–401. https://doi.org/10.1111/1754-9485.12556

4. Nabavizadeh N et al (2016) Image guided radiation therapy (IGRT) practice patterns and IGRT's impact on workflow and treatment planning: results from a National Survey of American Society for Radiation Oncology members. Int J Radiat Oncol Biol Phys 94(4):850–857. https://doi.org/10.1016/j.ijrobp.2015.09.035

5. Padayachee J, Loh J, Tiong A, Lao L (2017) National survey on image-guided radiotherapy practice in New Zealand. J Med Imaging Radiat Oncol 62(2):262–269. https://doi.org/10.1111/1754-9485.12682

6. Alaei P, Spezi E (2015) Imaging dose from cone beam computed tomography in radiation therapy. Phys Med 31(7):647–658. https://doi.org/10.1016/j.ejmp.2015.06.003

7. Murphy MJ et al (2007) The management of imaging dose during image-guided radiotherapy: report of the AAPM Task Group 75. Med Phys 34(10):4041–4063. https://doi.org/10.1118/1.2775667

8. Descamps C, Gonzalez M, Garrigo E, Germanier A, Venencia D (2012) Measurements of the dose delivered during CT exams using AAPM Task Group Report No. 111. J Appl Clin Med Phys. https://doi.org/10.1120/jacmp.v13i6.3934

9. Ding GX et al (2018) Image guidance doses delivered during radiotherapy: Quantification, management, and reduction: report of the AAPM Therapy Physics Committee Task Group 180. Med Phys 45(5):84–99. https://doi.org/10.1002/mp.12824

10. Rehani MM et al (2015) Radiological protection in cone beam computed tomography (CBCT). Ann ICRP 44(1):9–127. https://doi.org/10.1177/0146645315575485

11. de Las Heras Gala H et al (2017) Quality control in cone-beam computed tomography (CBCT) EFOMP-ESTRO-IAEA protocol. Phys Med 39:67–72. https://doi.org/10.1016/j.ejmp.2017.05.069

12. Luh JY et al (2020) ACR-ASTRO practice parameter for image-guided radiation therapy (IGRT). Am J Clin Oncol 43(7):459–468. https://doi.org/10.1097/COC.0000000000000697

13. National Health Service (NHS) (2012) National radiotherapy implementation group report: image guided radiotherapy (IGRT), guidance for implementation and use

14. International Atomic Energy Agency (IAEA) (2011) Status of computed tomography, dosimetry for wide cone beam scanners. In: IAEA human health reports, vol 5

15. Sykes JR, Lindsay R, Iball G, Thwaites D (2004) Dosimetry of CBCT: methods, doses and clinical consequences. J Phys 444:1013

16. Boone JM, Strauss KJ, Cody DD, McCollough CH, McNitt-Gray MF, Toth TL (2011) Report of AAPM TG 204: size-specific dose estimates (SSDE) in pediatric and adult body CT examinations. J Appl Clin Med Phys

17. Alvarado R, Booth JT, Bromley RM, Gustafsson HB (2013) An investigation of image guidance dose for breast radiotherapy. J Appl Clin Med Phys. https://doi.org/10.1120/jacmp.v14i3.4085

18. Wood TJ, Moore CS, Horsfield CJ, Saunderson JR, Beavis AW (2015) Accounting for patient size in the optimization of dose and image quality of pelvis cone beam CT protocols on the varian OBI system. Br J Radiol. https://doi.org/10.1259/bjr.20150364

19. Wood TJ, Moore CS, Saunderson JR, Beavis AW (2015) Validation of a technique for estimating organ doses for kilovoltage cone-beam CT of the prostate using the PCXMC 2.0 patient dose calculator. J Radiol Prot 35(1):153–163. https://doi.org/10.1088/0952-4746/35/1/153

20. Rampado O, Giglioli FR, Rossetti V, Fiandra C, Ragona R, Ropolo R (2016) Evaluation of various approaches for assessing dose indicators and patient organ doses resulting from radiotherapy cone-beam CT. Med Phys 43(5):2515–2526. https://doi.org/10.1118/1.4947129

21. Tapiovaara M, Siiskonen T (2008) PCXMC: a Monte Carlo program for calculating patient doses in medical x-ray examinations, 2nd edn. STUK, Helsinki

22. STUK PCXMC—a Monte Carlo program for calculating patient doses in medical X-ray examinations. STUK. Available at https://www.stuk.fi/palvelut/pcxmc-a-monte-carlo-program-for-calculating-patient-doses-in-medical-x-ray-examinations. Accessed on 2020

23. Australian Bureau of Statisticis (ABS) (1995) How Australians measure up, 1995. Australian Bureau of Statistics, Canberra

24. Commonwealth Scientific and Industrial Research Organisation (CSIRO) and University of South Australia (2007) Children's nutrition and physical activity survey: main findings. Australian Government, Canberra

25. Varian Medical Systems Inc (2018) On-board imager (OBI) reference guide. Varian Medical Systems Inc, Crawley

26. Siemens X-ray spectra simulation. Available at https://www.oem-products.siemens-healthineers.com/x-ray-spectra-simulation. Accessed on 01 Mar 2020

27. Wen N et al (2007) Dose delivered from Varian's CBCT to patients receiving IMRT for prostate cancer. Phys Med Biol 52(8):2267–2276. https://doi.org/10.1088/0031-9155/52/8/015

28. Kan M, Leung L, Wong W, Lam N (2008) Radiation dose from cone beam computed tomography for image-guided radiation therapy. Int J Radiat Oncol Biol Phys 70(1):272–279. https://doi.org/10.1016/j.ijrobp.2007.08.062

29. Osei EK, Schaly B, Fleck A, Charland P, Barnett R (2009) Dose assessment from an online kilovoltage imaging system in radiation therapy. J Radiol Prot 29(1):37–50. https://doi.org/10.1088/0952-4746/29/1/002

30. Ding GX, Duggan DM, Coffey CW (2007) Characteristics of kilovoltage x-ray beams used for cone-beam computed tomography in radiation therapy. Phys Med Biol 52(6):1595–1615. https://doi.org/10.1088/0031-9155/52/6/004

31. Song WY et al (2008) A dose comparison study between XVI and OBI CBCT systems. Med Phys 35(2):480–486. https://doi.org/10.1118/1.2825619

32. Tomic N, Devic S, DeBlois F, Seuntjens J (2010) Reference radiochromic film dosimetry in kilovoltage photon beams during CBCT image acquisition. Med Phys 37(3):1083–1092. https://doi.org/10.1118/1.3302140

33. ICRP (2007) The recommendations of the International Commission on radiological protection. ICRP publication. ICRP, Stockholm

34. Kench PL et al (2020) Imaging prior to radiotherapy impacts in-vitro survival. Phys Imaging Radiat Oncol 16:138–143. https://doi.org/10.1016/j.phro.2020.11.003